Numerical simulation of 3D flow in axial turbomachines

S. Yershov*, A. Rusanov*, A. Gardzilewicz**, P. Lampart**, J. Œwirydczuk**
* *Institute for Machine Construction, National Academy of Sciences of Ukraine, Kharkov*
** *Institute of Fluid Flow Machinery, Polish Academy of Sciences, Gdañsk,*

Abstract

The paper is intended to describe a method for the calculation of 3D viscous compressible (subsonic or supersonic) flow in axial turbomachines described in the form of thin-layer Reynolds-averaged Navier-Stokes equations. The method draws on Godunov-type upwind differencing and ENO reconstruction suggested by Harten so as to assure monotonicity preserving and high accuracy of computational results. The computational efficiency is achieved thanks to the implementation of a simplified H-type multi-grid approach and δ-form implicit step. Turbulent effects are simulated with the help of a modified algebraic model of Baldwin-Lomax. This method was at the foundation of a computer code - a complex software package to calculate 3D flow in multi-stage turbomachines that allows us to obtain local characteristics, like temperature, pressure, density or velocity distributions, as well as global characteristics, like flow rates, stage reaction, flow efficiency for the considered turbine/compressor stage. The paper also gives selected results of computation of a number of turbimachinery cascades, showing that these results agree reasonably well with the available experimental data.

I. Introduction

The 1990s have brought a rapid development of CFD (computational fluid dynamics) codes to solve 3D flows in a number of engineering applications, including turbomachinery. Results obtained from these codes facilitate design and analysis of turbomachinery performance that would otherwise have to be carried out by means of experimental testing, involving more cost, time and risk. Turbomachinery flows are well known to be a playground for several phenomena of gas dynamics which take place in extremely complex geometries, only to mention leakage, unsteadiness, turbulence, laminar-turbulent transition, separation, shock wave interaction, vortex flows. All these phenomena may have a considerable effect on the performance of turbomachinery and should be accounted for in what aspires to be a modern CFD code.

In this paper we will mainly concentrate on two aspects of CFD simulation, that is turbulence modelling and numerical resolution as these aspects are still in the centre of research. The choice of an appropriate turbulence model is an important problem for non-DNS (direct numerical simulation) codes. We make use of a modified Baldwin-Lomax turbulence model - an algebraic zero-equation model that has been tested to good effect in complex turbomachinery geometries and for its relative simplicity does not impose major difficulties in numerical implementation.

A numerical technique used in this paper can be called a Godunov-type ENO (essentially non-oscillatory) scheme. This approach was put forward by Yershov [24,25], who constructed this scheme based on theoretical ideas of essentially non-oscillatory schemes presented in a landmark paper of Harten & Osher [11], and then developed by Yershov & Rusanov [26,27,28, 29] into an application package known under the name **FlowER** for the computation of 3D viscous turbomachinery flows. It is believed that ENO schemes owing to their advantageous features of monotonicity preserving and high-order accuracy have an upper hand over central-difference schemes which are non-monotonous and non-linearly unstable without artificial diffusion, and also over TVD (total variation diminishing) schemes which, although monotonicity preserving, tend to degenerate to first-order accuracy at local extremes.

II. Governing equations.

Turbomachinery flows can be described by a set of thin-layer Reynolds-averaged unsteady Navier-Stokes equations written in a curvilinear body-fitted coordinate system (ξ,η,ζ) presented in Fig. 1 and rotating with an angular speed Ω. The idea of thin-layer approximation is to discard streamwise diffusive terms, compared to the full Navier-Stokes equations. The approximation is well-founded due to the fact that for high Reynolds numbers, terms containing second derivatives of the velocity in the

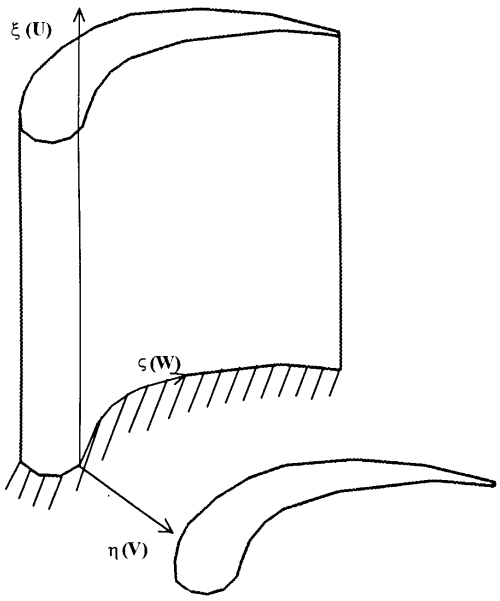

Fig. 1. A curvilinear coordinate system (ξ, η, ς) in a blade-to-blade passage.

streamwise direction are much lower than the derivatives in cross-stream directions and can be left out. This approach containing all Euler terms and cross-stream diffusion can be considered an intermediate step between full Navier-Stokes equations and boundary-layer approximation, and unlike the latter is capable of properly representing the effects of separation. The set of governing equations is presented below in matrix form

$$\frac{\partial QJ}{\partial t}+\frac{\partial E}{\partial \xi}+\frac{\partial F}{\partial \eta}+\frac{\partial G}{\partial \varsigma}=JH+\frac{\partial R_\xi}{\partial \xi}+\frac{\partial R_\eta}{\partial \eta}, \tag{1}$$

where Q is a conservative variable vector, E, F and G are flux vectors; H is a source term vector; R_ξ and R_η are cross-stream viscous terms which can be expressed as follows

$$Q=\begin{pmatrix}\rho\\ \rho u\\ \rho v\\ \rho w\\ h\end{pmatrix};\ R_\xi=\mu J\begin{pmatrix}0\\ \frac{1}{3}\sigma_\xi\xi_x+\xi_0^2\frac{\partial u}{\partial \xi}\\ \frac{1}{3}\sigma_\xi\xi_y+\xi_0^2\frac{\partial v}{\partial \xi}\\ \frac{1}{3}\sigma_\xi\xi_z+\xi_0^2\frac{\partial w}{\partial \xi}\\ \frac{1}{3}\sigma_\xi U+\xi_0^2\left(u\frac{\partial u}{\partial \xi}+v\frac{\partial v}{\partial \xi}+w\frac{\partial w}{\partial \xi}+\frac{1}{\mathrm{Pr}}\frac{\partial i}{\partial \xi}\right)\end{pmatrix}; \tag{2a}$$

$$R_\eta=\mu J\begin{pmatrix}0\\ \frac{1}{3}\sigma_\eta\eta_x+\eta_0^2\frac{\partial u}{\partial \eta}\\ \frac{1}{3}\sigma_\eta\eta_y+\eta_0^2\frac{\partial v}{\partial \eta}\\ \frac{1}{3}\sigma_\eta\eta_z+\eta_0^2\frac{\partial w}{\partial \eta}\\ \frac{1}{3}\sigma_\eta V+\eta_0^2\left(u\frac{\partial u}{\partial \eta}+v\frac{\partial v}{\partial \eta}+w\frac{\partial w}{\partial \eta}+\frac{1}{\mathrm{Pr}}\frac{\partial i}{\partial \eta}\right)\end{pmatrix};\ H=\begin{pmatrix}0\\ 2\rho v\Omega+\rho\Omega^2 r_x\\ -2\rho u\Omega+\rho\Omega^2 r_y\\ 0\\ 0\end{pmatrix}; \tag{2b}$$

$$E=J\begin{pmatrix}\rho U\\ \rho uU+p\xi_x\\ \rho vU+p\xi_y\\ \rho wU+p\xi_z\\ (h+p)U\end{pmatrix};\qquad F=J\begin{pmatrix}\rho V\\ \rho uV+p\eta_x\\ \rho vV+p\eta_y\\ \rho wV+p\eta_z\\ (h+p)V\end{pmatrix};\qquad G=J\begin{pmatrix}\rho W\\ \rho uW+p\varsigma_x\\ \rho vW+p\varsigma_y\\ \rho wW+p\varsigma_z\\ (h+p)W\end{pmatrix}; \tag{2c}$$

In the above formulas p is the pressure, u,v,w - Cartesian components of the velocity, U,V,W - contravariant components of the velocity, i - enthalpy given by

$$U=u\xi_x+v\xi_y+w\xi_z\ ;\ V=u\eta_x+v\eta_y+w\eta_z\ ;\ W=u\varsigma_x+v\varsigma_y+w\varsigma_z\ . \tag{3a}$$

$$i=\frac{\gamma}{\gamma-1}\frac{p}{\rho}\ ; \tag{3b}$$

and

$$h=\frac{p}{\gamma-1}+\rho\frac{u^2+v^2+w^2-\Omega^2r^2}{2}\ . \tag{3c}$$

The following symbols were introduced to describe viscous fluxes R_ξ and R_η

$$\xi_0 = \sqrt{\xi_x^2 + \xi_y^2 + \xi_z^2} \ ; \qquad \eta_0 = \sqrt{\eta_x^2 + \eta_y^2 + \eta_z^2} \ ; \tag{4a}$$

$$\sigma_\xi = \xi_x \frac{\partial u}{\partial \xi} + \xi_y \frac{\partial v}{\partial \xi} + \xi_z \frac{\partial w}{\partial \xi} \ ; \qquad \sigma_\eta = \eta_x \frac{\partial u}{\partial \eta} + \eta_y \frac{\partial v}{\partial \eta} + \eta_z \frac{\partial w}{\partial \eta} \ ; \tag{4b}$$

J denotes the Jacobian of the transformation from the Cartesian to curvilinear coordinate system

$$J = \det \mathrm{J} = \begin{pmatrix} \frac{\partial \xi}{\partial x}, \frac{\partial \eta}{\partial x}, \frac{\partial \varsigma}{\partial x} \\ \frac{\partial \xi}{\partial y}, \frac{\partial \eta}{\partial y}, \frac{\partial \varsigma}{\partial y} \\ \frac{\partial \xi}{\partial z}, \frac{\partial \eta}{\partial z}, \frac{\partial \varsigma}{\partial z} \end{pmatrix} = \det \begin{pmatrix} \xi_x, \eta_x, \varsigma_x \\ \xi_y, \eta_y, \varsigma_y \\ \xi_z, \eta_z, \varsigma_z \end{pmatrix} \tag{4c}$$

and γ is the specific heat ratio, Pr - Prandtl number, μ - effective (molecular and turbulent) viscosity as in the Bussinesq hypothesis

$$\mu = \mu_{lam} + \mu_{tur}, \tag{5a}$$

The laminar part in Eq. (5a) can be found from the formula of Sutherland as below

$$\mu = C_1 T^{1.5} / (T + C_2) \tag{5b}$$

where $T = \frac{p}{\rho R}$; $C_1 = 1.4458 \cdot 10^{-6} \frac{kg}{m \cdot s \cdot K^{0.5}}$; C_2=110.4 K and R is a gas constant.

In order to determine the turbulent part a modified Baldwin-Lomax model is used (see next paragraph). The effective heat conductivity can be described as

$$\frac{\mu}{Pr} = \frac{\mu_{lam}}{Pr_{lam}} + \frac{\mu_{tur}}{Pr_{tur}} \tag{5c}$$

assuming the laminar and turbulent Prandtl numbers as in the case of air, that is $Pr_{lam}=0.72, Pr_{tur}$=0.9.

At each nodal point of the calculation region, five unknowns are calculated from the set of Eqs. (1) - they are: three components of the velocity, density and pressure. Based on values of these parameters, other local characteristics, like temperature, enthalpy, or entropy distributions, as well as global characteristics, like flow rates, stage reaction or flow efficiency for a considered turbine (compressor) stage can be found.

As seen from Eqs. (3b) and (5b), thermodynamic parameters are linked by the state equation of perfect gas. The gas constant and specific heat ratio are assumed constant within the turbomachinery stage and do not depend on changes of pressure and temperature.

Boundary conditions

The following boundary conditions are assumed **at the inlet** to the computational domain

- span-wise distributions of total pressure, total temperature, pitch and yaw angles

$$p_{0t}=p_{0t}(r),\ T_{0t}=T_{0t}(r),\ \gamma = \gamma(r),\ \varphi = \varphi(r) \tag{6a}$$

- span-wise distribution of static pressure (voluntary as an additional condition to help evaluate the initial flow field)

$$p_{0s}=p_{0s}(r). \tag{6b}$$

There are several boundary conditions to be imposed optionally **at the exit** from the computational domain (all these conditions have already been tested)
- span-wise distribution of static pressure

$$p_2=p_2\,(r) \tag{7a}$$

- static pressure at the mid-span section p_2; the span-wise distribution of static pressure is calculated then from the radial equilibrium equation

$$\frac{1}{r}\frac{dp}{dr}=\frac{Cu^2}{r} \tag{7b}$$

- mass flow rate G or volumetric flow rate G_V. These boundary conditions are recommended for low flow-rate compressor throughflows. For both cases, the span-wise distribution of static pressure can be calculated either from the left Riemann invariant $I^- = w - \frac{2}{\gamma-1}\sqrt{\gamma p/\rho}$ kept constant, or from the radial equilibrium equation, for details see [28].

At the walls (blade surface or endwalls) the following boundary conditions are assumed
- no-slip

$$U = V = W = 0 \tag{8a}$$

- wall temperature or (no) heat flux at the wall

$$T_W = const, \text{ or } \frac{\partial T}{\partial \eta} = const \tag{8b}$$

The static pressure is calculated from Eq. (1) written along cross-flow gridlines as below
- at blade walls

$$\frac{\partial p}{\partial \eta}=\frac{1}{J}\left\{\left(\frac{1}{3}+\eta_0^2\right)\mu\frac{\partial}{\partial\eta}\left[\frac{\partial(JV)}{\partial\eta}\right]+\left(x_\xi x_\eta+y_\xi y_\eta+z_\xi z_\eta\right)\cdot\frac{\partial}{\partial\eta}\left[\eta_0^2\mu\frac{\partial(JU)}{\partial\eta}\right]\right.$$
$$\left.+\left(x_\eta x_\xi+y_\eta y_\xi+z_\eta z_\xi\right)\frac{\partial}{\partial\eta}\left[\eta_0^2\mu\frac{\partial(JW)}{\partial\eta}\right]\right\} \tag{8c}$$

- at endwalls

$$\frac{\partial p}{\partial \xi}=\frac{1}{J}\left\{\left(\frac{1}{3}+\xi_0^2\right)\mu\frac{\partial}{\partial\xi}\left[\frac{\partial(JU)}{\partial\xi}\right]+\left(x_\xi x_\eta+y_\xi y_\eta+z_\xi z_\eta\right)\cdot\frac{\partial}{\partial\xi}\left[\xi_0^2\mu\frac{\partial(JV)}{\partial\xi}\right]+\right.$$
$$\left.+\left(x_\eta x_\xi+y_\eta y_\xi+z_\eta z_\xi\right)\frac{\partial}{\partial\xi}\left[\xi_0^2\mu\frac{\partial(JW)}{\partial\xi}\right]\right\} \tag{8d}$$

III. Modelling turbulence

The simulation of turbulent effects is of great importance for the computation of three-dimensional viscous turbomachinery flows. There is a number of turbulence models ranging from simple algebraic to differential Reynolds stress models. None of them is capable of correctly describing all types of

flows. Therefore, it is crucial that a chosen model should be appropriate for the investigated flow and easy to implement without considerably increasing computational costs. The model used in the paper is a modified Baldwin-Lomax model - an algebraic two-layer eddy-viscosity model put forward originally in [1].

The main idea of this model is to divide the boundary layer into two domains - an inner and outer layer, as shown in Fig. 2.

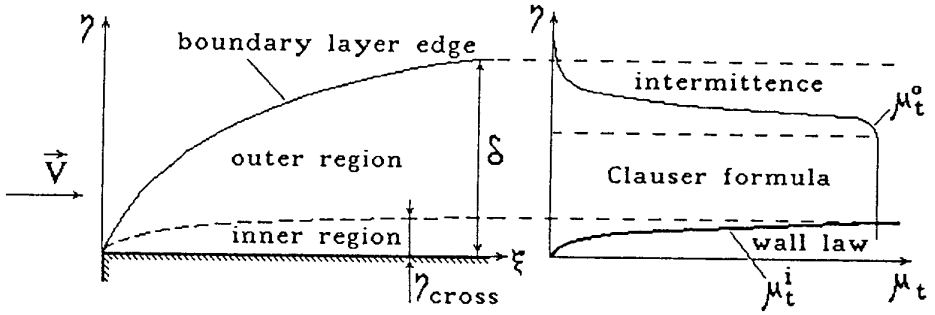

Fig. 2. The calculation of turbulent viscosity in the boundary layer.

The Prandtl concept of mixing length is used in the inner region to calculate the distribution of turbulent viscosity

$$\mu_{turb} = \mu^{i}_{turb} = \rho l^2 |\vec{\omega}|; \tag{9a}$$

where ω is the vorticity, l - a mixing length, that is a linear scale of turbulence calculated as

$$l = ky\left[1 - \exp\left(-\eta^{+} / A^{+}\right)\right]; \tag{9b}$$

where η is a distance from the wall; - $\eta^{+} = \eta\sqrt{\rho_w / \tau_w} / \mu_w$ non-dimensional distance, τ_w - wall shear stress, k=0.4 - Karman constant; A^{+} = 26 - van Driest constant.

The eddy viscosity in the outer region of the boundary layer is defined by the modified Clauser formula

$$\mu_{turb} = \mu^{0}_{turb} = \alpha\, C_{CP}\, \rho F_{WK} F_k \; ; \tag{10a}$$

Subsequent terms of this equation are explained as

$$\alpha = K_{CL}\frac{1.55}{1+\varphi}, \quad \varphi = 0.55\left[1 - \exp\left(-0.243\sqrt{z} - 0.298\, z\right)\right] \tag{10b}$$

where z=Re_θ/425 - 1, K_{CL} = 0.0168 - Clauser constant,

$\mathrm{Re}_\theta = \dfrac{\rho U \theta}{\mu}$ - momentum thickness Reynolds number;

It is assumed that C_{CP} = 1.6. F_{WK} is the wake function expressed as follows

$$F_{wk} = \min(\eta_{\max} F_{\max}\ , C_{WK}\eta_{\max} U_D^2 / F_{\max}) \tag{10c}$$

where U_d = U_{max} - U_{min} is the difference between the maximum and minimum velocity at the boundary layer section; C_{WK} = 0.25 is the wake constant. $F_{\max}$ is a maximum of the velocity function

$$F(\eta) = \eta|\vec{\omega}|\left[1 - \exp\left(\eta^{+} / A^{+}\right)\right]. \tag{10d}$$

whereas η_{max} is the coordinate that refers to that maximum location.

F_K in Eq. (10a) is the Klebanoff intermittency factor given by

$$F_k = \left[1 + 5.5\left(C_k \eta / \eta_{\max}\right)^6\right]^{-1} \tag{10e}$$

where $C_k = 0.3$ is the Klebanoff constant.

The division between the inner and outer layer is assumed at a point nearest to the wall where

$$\mu^i_{turb} = \mu^0_{turb} . \tag{11}$$

The model does not explain the phenomena of laminar-turbulent transition. The flow is assumed turbulent if at some point of the boundary layer profile the turbulent viscosity calculated as prescribed above is 14 time larger than the molecular viscosity of undisturbed flow. Otherwise, the boundary layer is thought to be laminar at this section.

The original model of Baldwin-Lomax as described above has been modified by Yershov & Rusanov [30] so as to correct its weak points. Main problems are connected with the calculation of turbulent viscosity in the regions of separation and wake.

Usually, the turbulent viscosity calculated in separated flows is too low and according to the criterion given above the flow is predicted laminar. This in turn will increase dimensions of the laminar recirculation zone. Furthermore, if the flow is supersonic, the oversized recirculation zone will intensify the compression wave near the separation and the separation point will move upstream. This will further decrease the turbulent viscosity and extend the recirculation zone. In the light of the above, several measures were taken to improve the computational conditions. First, the velocity U_{min} was assumed as a negative of the maximum backflow velocity, unlike in the original Baldwin-Lomax where U_{min}=0. Second, following [15] the value of coefficient C_W in the recirculation zone was increased according to the formula below

$$C_W = C_W^{BL}\left(1 + D_W \eta_{sep} / L\right); \tag{12}$$

where C_W^{BL} is the wake constant in the original Baldwin-Lomax model; η_{sep} - backflow thickness; L - characteristic dimension (blade span for endwall boundary layers or pitch for boundary layers at blade walls), $D_W \approx 50$. Next, in the proximity of separation and reattachment the wall shear stress τ_w tends to zero and the model may yield unphysical values of turbulent viscosity. Therefore, following [4] one can replace the wall shear stress in the separation region with an averaged value defined as

$$\overline{\tau}_w = \frac{1}{L(\xi)} \int_0^L \tau_w(\xi)\, d\xi, \tag{13}$$

where ξ is the curvilinear body-fitted coordinate, L - is a distance along the wall. In order to assure smooth changes of turbulent viscosity, the flow history is taken into account using a simple relaxation procedure that refers to turbulent viscosity upstream, see [5]:

$$\mu_{t_i} = (1 - \chi)\widetilde{\mu}_{t_i} + \chi \mu_{t_{i-1}} . \tag{14}$$

where μ_{t_i} is the resultant turbulent viscosity coefficient, $\widetilde{\mu}_{t_i}$ - its preliminary value, $\mu_{t_{i-1}}$ - turbulent viscosity one cell upstream, χ=0.1-0.3 is the correlation coefficient.

The original Baldwin-Lomax model simulates poorly eddy-viscosity in wakes. For far wakes usually the Clauser formulation is assumed

$$\mu_{CL} = \widetilde{K}_{CL}\, \rho U_e\, \delta^*\, \widetilde{F}_K , \tag{15a}$$

where δ^* is the displacement thickness, U_e is the outer flow velocity. As it is difficult to determine the displacement thickness for an arbitrary three-dimensional wake, usually the constancy of the maximum turbulent viscosity as well as the constancy of the quantity $\rho U_e \delta^*$ is assumed which reduces Eq. (15a) to the form

$$\mu_{CL} = \max_{\eta}(\mu_{te})\widetilde{F}_K \,. \tag{15b}$$

where μ_{te} is the turbulent viscosity at the trailing edge. $\widetilde{F}_K$ is the Klebanoff intermittency factor

$$\widetilde{F}_k = \left[1 + 5.5\left(\eta / \widetilde{\delta}\right)^6\right]^{-1} \tag{15c}$$

where the wake thickness $\widetilde{\delta}$ is estimated as

$$\widetilde{\delta} = \min(\eta_{\max} / C_k, 2\delta_\omega), \tag{15d}$$

and δ_ω is a cross-wake distance between the wake axis and a point in the wake where the vorticity assumes a maximum value. The relation $\widetilde{\delta} \approx 2\delta_\omega$ is usually valid. The wake axis is determined as a line that consists of points where the velocity is minimal and the entropy function reaches its maximum.
For a near wake the following relaxation formula is applied [21]

$$\mu_{turb} = \mu_{CL} + (\mu_{te} - \mu_{CL})\, exp[-\xi/(20\delta_{te})] \tag{16}$$

where μ_{CL}, μ_{te}, μ_{turb} are coefficients of turbulent viscosity calculated in the wake from the Clauser formula, calculated at the trailing edge from the Baldwin-Lomax model, and the resultant turbulent viscosity in the near wake, respectively. In Eq. (16) ξ is the distance from the trailing edge section and δ_{te} is the trailing edge boundary layer thickness.

The original Baldwin-Lomax turbulence model was put forward for 2D flow simulation. In order to implement it in 3D computations it is necessary to devise a procedure that accounts for intersecting effects of different walls (endwalls and blade walls). This procedure is as follows. For each point of a section $\zeta = const$ two coefficients of turbulent viscosity μ_{turb}^{ξ} (due to endwall effects) and μ_{turb}^{η} (due to blade wall effects) are calculated for independent length scales. Then, the final turbulent viscosity is found as a weighted average value as explained below. Both the blade-to-blade region and the wake region are divided into several sub-regions, see Fig. 3.

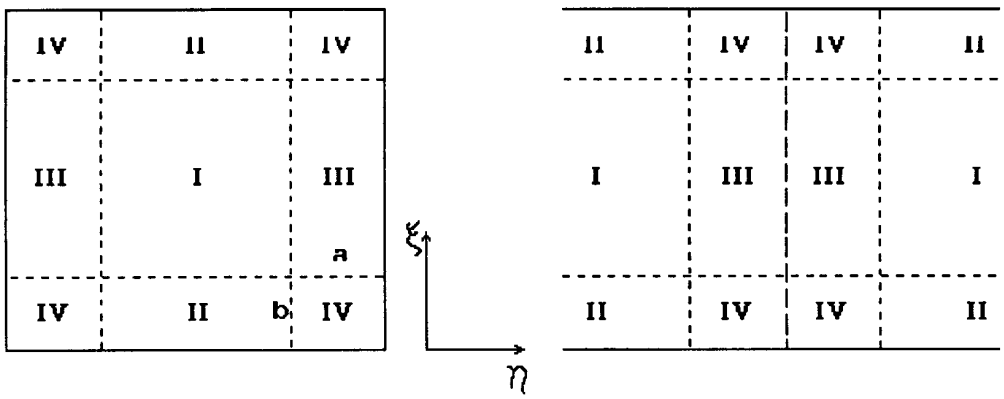

Fig. 3. The division of the blade-to-blade region (left) and the wake region (right) into several sub-regions for the calculation of turbulent viscosity coefficient.

In a section ζ = *const* of the blade-to-blade region one can distinguish the following sub-regions: I - outer flow, II - endwall boundary layers III - blade wall boundary layers, IV - corner boundary layers. In the sub-region I the coefficient of turbulent viscosity μ_{turb} is calculated as an average of μ^{ξ}_{turb} and μ^{η}_{turb} weighted according to the distance from the walls

$$\mu_{turb} = \frac{\mu^{\xi}_{turb} l_{\eta} + \mu^{\eta}_{turb} l_{\xi}}{l_{\eta} + l_{\xi}}. \tag{17a}$$

where l_{ξ}, l_{η} are distances from the endwall or blade wall, respectively. In the sub-region II μ_{turb} is assumed equal to μ^{ξ}_{turb}, whereas in III - equal to μ^{η}_{turb}. In the sub-region IV μ_{turb} is also evaluated as a weighted average of μ^{ξ}_{turb} and μ^{η}_{turb} taking into account the distances from the walls and sub-region boundaries

$$\mu_{turb} = \frac{\overline{\mu}^{\eta}_{turb}\Delta\eta + \overline{\mu}^{\xi}_{turb}\Delta\xi}{\Delta\eta + \Delta\xi}, \tag{17b}$$

where

$$\overline{\mu}^{\eta}_{turb} = \mu^{\eta}_{turb}\frac{\delta_{\xi} - \Delta\xi}{\delta_{\xi}}, \overline{\mu}^{\xi}_{turb} = \mu^{\xi}_{turb}\frac{\delta_{\eta} - \Delta\eta}{\delta_{\eta}}. \tag{17c}$$

The symbols used in Eqs. (17b, 17c) are easily explained with the help of Fig. 4.

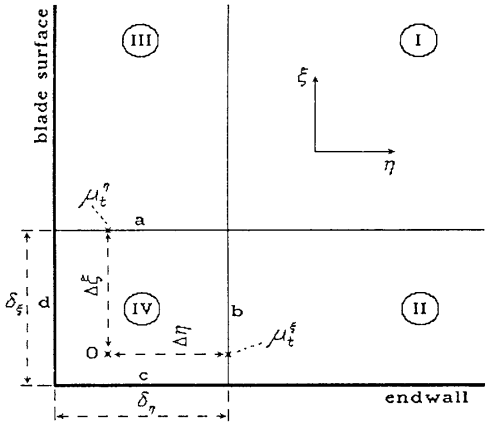

Fig. 4. Turbulent viscosity calculation in the corner sub-region.

In a section ζ = *const* of the wake region one can have the sub-regions: I - outer flow, II - endwall boundary layers III - wake / outer flow interaction, IV - wake / endwall boundary layer interaction. The calculation procedure is the same as above, bearing in mind that in order to determine μ^{η}_{turb}, we use the wake formula (15) instead of the wall formula (9).

IV. Numerical scheme

The matrix of governing equations (1) forms a set of complex non-linear partial differential equations. Neither an analytical solution has been found nor even the problem of existence and uniqueness of solution has yet been resolved and there is little hope that this problem will ever be resolved. The difficulties lie in non-linearity of equations, a large number of unknowns and geometrical complexity of boundaries. All hopes are pinned on numerical analysis and experimental validation of obtained numerical results. Although a considerable progress in quality of numerical schemes for Navier-Stokes and Euler solvers has been made over recent years (only to mention central difference schemes of MacCormack [19], Beam-Warming [2], Runge-Kutta resolution by Jameson

[18], upwind difference schemes of Godunov [9], modified by Ko³gan [16] and Tiliajeva [22], TVD schemes of Harten [10], Ramsey [20], Chakravarthy [3] and Nigmatullin [14]), further extensive research is required to make the numerical schemes stand up to what is deemed as fundamental criteria for their operation, that is accuracy, monotonicity preserving, proper approximation of convective derivatives, reliability and relatively low calculation costs. It is generally accepted that the schemes based on central differences generate non-linear instabilities wherever flow gradients become large and only upwind differencing assures linear and non-linear stability. In turn, Godunov-type and TVD schemes, although monotonicity preserving, with upwind differencing, and usually second-order accurate, tend to degenerate to first-order accuracy. The numerical scheme described in this paper is a modified upwind difference Godunov-type scheme that makes use of ENO reconstruction to approximate convective derivatives and assures at least second-order accuracy everywhere. This approach was put forward by Yershov [24,25,27,28], who constructed this scheme based on theoretical ideas of ENO schemes presented in a landmark paper of Harten & Osher [11].

Explicit step

The applied scheme draws on cell-centred finite-volume discretisation. The set of governing equations can be integrated in an elementary cell $\varphi_{i,j,k}$

$$\iiint\limits_{\phi_{i,j,k}} \frac{\partial Q J}{\partial t} d\phi + \iiint\limits_{\phi_{i,j,k}} \left[\frac{\partial (E - R_\xi)}{\partial \xi} + \frac{\partial (F - R_\eta)}{\partial \eta} + \frac{\partial G}{\partial \varsigma} \right] d\phi = \iiint\limits_{\phi_{i,j,k}} JH d\phi \tag{18}$$

Making use of the Gauss theorem with regards to the second integral, then taking into consideration the mean value theorem, one can obtain the following difference equation

$$\delta Q^n_{i,j,k} = Q^{n+1}_{i,j,k} - Q^n_{i,j,k} = -\frac{\tau}{(\Delta\xi \Delta\eta \Delta\varsigma J)_{i,j,k}} \left\{ \left[(E - R_\xi)^n \Delta\eta \Delta\varsigma \right]_{i+1/2,j,k} - \left[(E - R_\xi)^n \Delta\eta \Delta\varsigma \right]_{i-1/2,j,k} + \right.$$

$$\left. + \left[(F - R_\eta)^n \Delta\xi \Delta\varsigma \right]_{i,j+1/2,k} - \left[(F - R_\eta)^n \Delta\xi \Delta\varsigma \right]_{i,j-1/2,k} + \left[G^n \Delta\xi \Delta\eta \right]_{i,j,k+1/2} - \left[G^n \Delta\xi \Delta\eta \right]_{i,j,k-1/2} \right\} +$$

$$+ \tau H^{n+1/2}_{i,j,k} \tag{19}$$

(where subscripts *i,j,k* refer to cell centres, *i±1/2, j±1/2, k±1/2* - to cell sides and *n* is a time instant.

ENO approximation

In Godunov-type schemes the inviscid fluxes are found from the solution of the Riemann problem, that is the problem of finding gas dynamics parameters at a cell side (surface of discontinuity of parameters) based on their values in the neighbouring cells. In the case of weak flow gradients, a subsonic linear approximation is used. For large gradients the scheme relies on an iterative procedure depending on the velocity jump normal to the cell side. The Riemann problem solver is described in detail in [9] and assures upwind differencing. In the original Godunov scheme, the boundary values for the Riemann problem are taken as those of the cell centres. In the method presented in this paper the initial values for the Riemann problem are calculated from a time-space piece-wise linear extrapolation

$$q(\xi, \eta, \varsigma, t) = q_m + \left(\frac{\partial q}{\partial \xi} \right)_m (\xi - \xi_m) + \left(\frac{\partial q}{\partial \eta} \right)_m (\eta - \eta_m) + \left(\frac{\partial q}{\partial \varsigma} \right)_m (\varsigma - \varsigma_m) + \left(\frac{\partial q}{\partial t} \right)_n (t - t_n); \tag{20}$$

where $q = (\rho, u, v, w, p)$ is the primitive variable vector, q_m - its value at the cell centre, ξ_m, η_m, ζ_m - cell centre coordinates.

The spatial derivatives that appear in Eq. (20) are found from the following algorithm.

1. First, the primitive variables q are transformed into characteristic variables defined as

$$\Delta_m \varphi = L_\psi \Delta_m q \,, \tag{21}$$

where L_ψ is the matrix of left eigenvectors of a matrix D_ψ that appears in the non-divergent form of Eq. (1), see Eq. (25) below. The symbol ψ denotes any of the coordinates ξ, η, ζ; $\Delta_m q = q_m - q_{m-1}$ and $\Delta_m \phi = \phi_m - \phi_{m-1}$.

2. Then, the ENO approximation is used to define the derivatives of the characteristic variable vector

$$\left(\frac{\partial \phi}{\partial \psi}\right)_m \overset{def}{=} \frac{1}{\Delta\psi} \min \mathrm{mod}\Big[\Delta_m \varphi + \alpha \min \mathrm{mod}\big(\Delta_m \varphi - \Delta_{m-1}\varphi, \Delta_{m+1}\varphi - \Delta_m \varphi\big), \Delta_{m+1}\varphi - \beta \min \mathrm{mod}\big(\Delta_{m+1}\varphi - \Delta_m \varphi, \Delta_{m+2}\varphi - \Delta_{m+1}\varphi\big)\Big]; \tag{22a}$$

where $\Delta\psi$ is the cell size and the function **minmod** is defined as follows

$$\mathrm{minmod}(a,\ b) = \mathrm{sign}(a)\ \max\{0,\ \min[\,|a|, b\,\mathrm{sign}(a)]\}. \tag{22b}$$

The choice of constants α, β determines the order of the numerical scheme. For α=0; β=0 we have a classical TVD scheme that is locally second-order accurate. For α=1/2; β=1/2 we have an ENO scheme that is second-order accurate everywhere in time and space and does not degenerate to first-order accuracy at critical points. For α=2/3; β=1/3 the scheme is locally third-order accurate, remaining at least second-order everywhere. This scheme is implemented in the present paper to solve turbomachinery flows.

3. In order to finally find the derivatives of primitive variables an inverse transformation is used

$$\left(\frac{\partial q}{\partial \psi}\right)_m = L_\psi^{-1} \left(\frac{\partial \phi}{\partial \psi}\right)_m . \tag{23}$$

The operation of transformation from primitive to characteristic variables to calculate the derivatives in Eq. (20) has a stabilising effect on the calculation process as it prevents entropy drops usually responsible for failure to converge at the front of shock waves.

Let us remark that Eq. (22a) is written for cells of equal dimensions. However, grids used for computation of fluid domains are usually refined near the walls. In the present approach, we make use of an H-type body-fitted grid refined at the walls and near leading and trailing edges. Therefore, the formula (22a) should be improved to account for different cell dimensions

$$\left(\frac{\partial \varphi}{\partial \psi}\right)_m \overset{def}{=} \min \mathrm{mod}\left\{\frac{\Delta_m \varphi}{\Delta \psi_m} + \vartheta_1\big(\Delta_m \psi + \vartheta_2 \Delta_{m+1/2}\psi\big) \min \mathrm{mod}\left[\frac{\Delta_{m+1}\varphi - \Delta_m \varphi}{\Delta_m \psi^2}, \frac{\Delta_m \varphi - \Delta_{m-1}\varphi}{\Delta_{m-1}\psi^2}\right], \frac{\Delta_{m+1}\varphi}{\Delta_{m+1}\psi} + \vartheta_1\big(\Delta_{m+1}\psi - \vartheta_2 \Delta_{m+1/2}\psi\big) \min \mathrm{mod}\left[\frac{\Delta_{m+1}\varphi - \Delta_m \varphi}{\Delta_m \psi^2}, \frac{\Delta_{m+2}\varphi - \Delta_{m+1}\varphi}{\Delta_{m+1}\psi^2}\right]\right\} \tag{24}$$

where $\Delta_{m+1/2}\psi$ is the cell size, $\Delta_m \psi$ - distance between centres of neighbouring cells ($\Delta_{m-1/2}\psi + \Delta_{m+1/2}\psi = 2\Delta_m \psi$) and ϑ_1=1/2; ϑ_2=1/3.

The time derivative in Eq. (20) is found from the non-divergent form of the governing equations

$$J\frac{\partial q}{\partial t}+D_\xi\frac{\partial q}{\partial \xi}+D_\eta\frac{\partial q}{\partial \eta}+D_\varsigma\frac{\partial q}{\partial \varsigma}=T\left(JH+\frac{\partial R_\xi}{\partial \xi}+\frac{\partial R_\eta}{\partial \eta}\right) \tag{25a}$$

where matrices D_ψ can be found from Eq. (1)

$$D_\psi=\begin{vmatrix} U_\psi & \rho\psi_x & \rho\psi_y & \rho\psi_z & 0 \\ 0 & U_\psi & 0 & 0 & \psi_x/\rho \\ 0 & 0 & U_\psi & 0 & \psi_y/\rho \\ 0 & 0 & 0 & U_\psi & \psi_z/\rho \\ 0 & \gamma\rho\psi_x & \gamma\rho\psi_y & \gamma\rho\psi_z & U_\psi \end{vmatrix} \tag{25b}$$

U_ψ is one of *U,V,W; T* is a matrix of transformation from primitive to conservative variables.

The viscous fluxes are calculated based on ENO approximation of derivatives of the primitive variables (already done while evaluating the inviscid fluxes) and a weighted linear interpolation. For example, a quantity $\mu\left(\frac{\partial u}{\partial \eta}\right)$ at a cell side ξζ can be found from

$$\left(\mu\frac{\partial u}{\partial \eta}\right)_{j+1/2}=(\eta_{j+1/2}-\eta_j)\left(\mu\frac{\partial u}{\partial \eta}\right)_{j+1}+(\eta_{j+1}-\eta_{j+1/2})\left(\mu\frac{\partial u}{\partial \eta}\right)_j \tag{26}$$

Subscripts *i,k* are left out in Eq. (26) as constant. This approach ensures second-order accuracy and it is simpler and more natural than traditional central-difference approximations. The viscous terms are limited by the function **minmod** and the effects of viscosity are not distorted by unphysical numerical phenomena.

Implicit scheme

One drawback of the described explicit scheme is its insufficient effectiveness in terms of computational costs. The process of convergence to a steady-state solutions can be accelerated if an implicit scheme is applied. A number of implicit schemes have been elaborated to work with the Godunov scheme. In the present paper we make use of an implicit δ-operator of Beam & Warming [2]. This method can be considered supplementary to the explicit scheme and does not involve major changes in the concept of the algorithm.

In the construction of the implicit δ-operator of Beam & Warming the following asymptotic relation is used

$$\left[I+\frac{\theta}{(1+x)J}\left(\frac{\partial}{\partial \xi}A+\frac{\partial}{\partial \eta}B+\frac{\partial}{\partial \varsigma}C\right)\right]\delta Q^n=\frac{1}{1+x}RHS^n+\frac{x}{1+x}\delta Q^{n-1}, \tag{27}$$

where $I = diag\{1\}$ - unit matrix; θ and x - constants; *RHS* - right hand side of Eq. (25a). In order to obtain second-order accuracy it is necessary to put down $\theta = 2,\ x = 1$, and assure the approximation of *RHS* with second-order accuracy in space. The process of solving Eq. (27) requires its factorisation (with regards to space coordinates) and diagonalisation of matrices *A,B,C.*

In general, the applied implicit scheme is as follows

1) transformation to primitive variables

$$\delta q^n=\frac{1}{1+x}T\,\delta Q^n+\frac{x}{1+x}\delta q^{n-1}; \tag{28a}$$

2) transformation to characteristic variables with regards to coordinate ξ

$$\delta\varphi_{\xi}^{n} = L_{\xi}\delta q^{n}; \tag{28b}$$

3) implicit step with regards to ξ

$$\left[I + \frac{\tau\theta}{(1+x)J}\frac{\partial}{\partial\xi}\left(\Lambda_{\xi}^{+} + \Lambda_{\xi}^{-}\right)\right]\delta\varphi_{\xi}^{n+1/3} = \delta\varphi_{\xi}^{n}; \tag{28c}$$

4) inverse transformation to primitive variables

$$\delta q^{n+1/3} = L_{\xi}^{-1}\delta\varphi_{\xi}^{n+1/3} \tag{28d}$$

5) transformation to characteristic variables with regards to coordinate η

$$\delta\varphi_{\eta}^{n+1/3} = L_{\eta}\delta q^{n+1/3} \tag{28e}$$

6) implicit step with regards to η

$$\left[I + \frac{\tau\theta}{(1+x)J}\frac{\partial}{\partial\eta}\left(\Lambda_{\eta}^{+} + \Lambda_{\eta}^{-}\right)\right]\delta\varphi_{\eta}^{n+2/3} = \delta\varphi_{\eta}^{n+1/3}; \tag{28f}$$

7) inverse transformation to primitive variables

$$\delta q^{n+2/3} = L_{\eta}^{-1}\delta\varphi_{\eta}^{n+2/3} \tag{28g}$$

8) transformation to characteristic variables with regards to coordinate ζ

$$\delta\varphi_{\varsigma}^{n+2/3} = L_{\varsigma}\delta q^{n+2/3} \tag{28h}$$

9) implicit step with regards to ζ

$$\left[I + \frac{\tau\theta}{(1+x)J}\frac{\partial}{\partial\varsigma}\left(\Lambda_{\varsigma}^{+} + \Lambda_{\varsigma}^{-}\right)\right]\delta\varphi_{\varsigma}^{n} = \delta\varphi_{\varsigma}^{n+2/3}; \tag{28i}$$

10) inverse transformation to primitive variables

$$\delta q^{n} = L_{\varsigma}^{-1}\delta\phi_{\varsigma}^{n} \tag{28j}$$

11) calculation of primitive variables in a subsequent time step *n+1*

$$q^{n+1} = q^n + \delta q^n . \tag{28k}$$

The derivatives in Eqs. (2.67), (2.70) and (2.73) are substituted with upwind differences, for example

$$\left[\frac{\partial}{\partial\psi}\left(\Lambda_\psi^+ + \Lambda_\psi^-\right)\right]_m \delta\varphi_\psi = \frac{\Delta_m \Lambda_\psi^+ \delta\varphi_\psi}{\Delta_m \psi} + \frac{\Delta_{m+1}\Lambda_\psi^- \delta\varphi_\psi}{\Delta_{m+1}\psi} \tag{28l}$$

In the above formulas the symbols $\Lambda_\psi^\pm$ are defined as

$$\Lambda_\psi^\pm = \frac{\Lambda_\psi \pm \left|\Lambda_\psi\right|}{2}, \tag{28m}$$

where the diagonal matrix Λ_ψ consists of eigenvalues of D_ψ

$$\Lambda_\psi = L_\psi D_\psi L_\psi^{-1} \tag{28n}$$

obtained from D_ψ through diagonalisation, using matrices L_ψ, L_ψ^{-1} whose columns are left and right, respectively, eigenvectors of D_ψ. The diagonal matrix $\left|\Lambda_\psi\right|$ consists of absolute values

$$\left|\Lambda_\psi\right| = diag\left\{\left|\Lambda_\psi\right|\right\}. \tag{28o}$$

Mixing plane

The elaborated method enables the calculation of one-stage and multi-stage turbomachines, including both stationary and rotating blade rows that are calculated in coordinate systems fixed to the blading (rotating with the rotational speed of blade rows). The stator/rotor interaction is accounted for through exchange of averaged thermodynamic parameters. This mixing procedure is accomplished in the gap between the blade rows with the help of non-reflective boundary conditions to prevent reflection of waves there. The non-divergent form of Eq. (25a) is rewritten as

$$J\frac{\partial q}{\partial t} + D_\xi \frac{\partial q}{\partial \xi} + D_\eta \frac{\partial q}{\partial \eta} + D_\varsigma^+ \frac{\partial q}{\partial \zeta} + D_\varsigma^- \frac{\partial q}{\partial \zeta} = T\left(JH + \frac{\partial R_\xi}{\partial \xi} + \frac{\partial R_\eta}{\partial \eta}\right). \tag{29a}$$

where matrices $D_\psi^\pm$ are given by

$$D_\psi^\pm = L_\psi^{-1} \Lambda_\psi^\pm L_\psi \tag{29b}$$

Non-reflective conditions are obtained assuming that at the inlet to a non-first blade row $D_\varsigma^+ \frac{\partial q}{\partial \zeta} = 0$; at the exit from a non-last blade row $D_\varsigma^- \frac{\partial q}{\partial \zeta} = 0$. Then, Eq. (29a) reduces to

$$J\frac{\partial q}{\partial t} + D_\xi \frac{\partial q}{\partial \xi} + D_\eta \frac{\partial q}{\partial \eta} + D_\varsigma^\pm \frac{\partial q}{\partial \zeta} = T\left(JH + \frac{\partial R_\xi}{\partial \xi} + \frac{\partial R_\eta}{\partial \eta}\right). \tag{30}$$

Therefore, the following numerical procedure to evaluate primitive variables at non-first inlet / non-last exit sections is assumed

$$\delta q^{n+1} = \delta q^n + \tau\left\{TH - \frac{1}{J}\left(A\frac{\partial q}{\partial \xi} + B\frac{\partial q}{\partial \eta} + D_\varsigma^\pm \frac{\partial q}{\partial \zeta}\right)\right\},$$

where $\delta q = q - q_0$; q_0 - circumferentially averaged primitive variable vector. The derivatives $\frac{\partial q}{\partial \xi}, \frac{\partial q}{\partial \eta}, \frac{\partial q}{\partial \zeta}$

are calculated from ENO approximation and inviscid fluxes are found with the help of the Riemann problem solver.

V. Numerical results

Langston cascade

Our first example of numerical calculations refers to a 3D linear cascade investigated experimentally by Langston et al. [17]. The exit Mach number was about 0.2, Reynolds number - 500 000. The calculated velocity vectors near the endwall of the Langston cascade are presented in Fig. 5a and exhibit the presence of a horseshoe vortex generated near the leading edge that consists of two branches. One branch passes around the leading edge and propagates at the suction side of the blade, the other spreads through the passage to the suction side of the neighbouring blade. The surface streamline that divides the passage and corner vortices can be seen near the suction side of the blade. The corresponding experimental endwall flow obtained by Langston is displayed in Fig. 5b. The comparison of computational and experimental static pressure contours is shown in Figs. 6a and 6b.

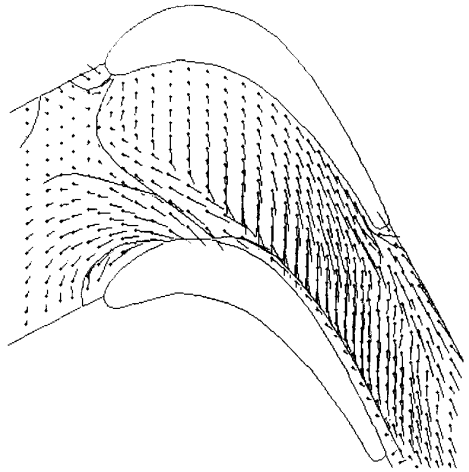

Fig.5a. Langston cascade - computed velocity vectors at the endwall.

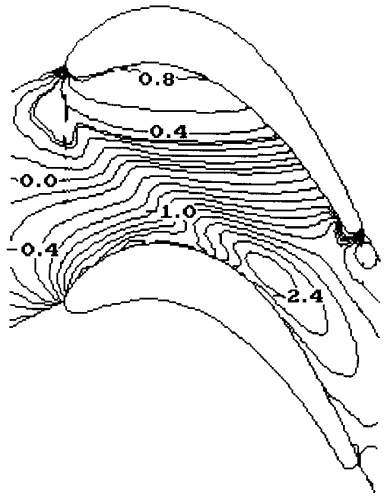

Fig.6a. Langston cascade - computed total pressure contours at the endwall.

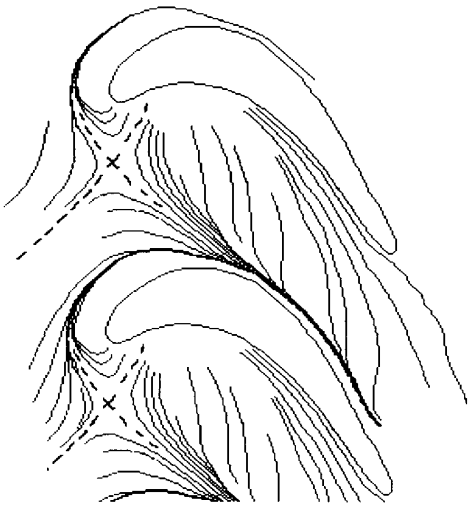

Fig.5b. Langston cascade - experimental endwall flow.

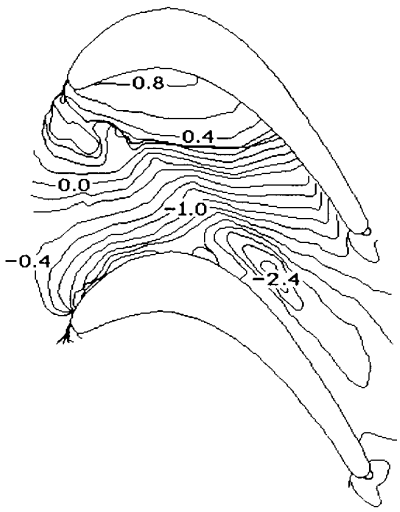

Fig.6b. Langston cascade - experimental total pressure contours at the endwall.

The next pictures shown in Fig. 7 illustrate computational and experimental contours of the total pressure coefficient at cross-flow sections of the blade-to-blade passage for several distances

from the leading edge - 14, 55, 96% axial chord. These pictures show subsequent stages of development of secondary flow structures that evolve from the horseshoe vortices. A similar secondary vortex is conspicuous in Fig. 8 that displays contours of the static pressure coefficient in the blade-to-blade passage at 82% axial chord from the leading edge. Although, the computed results can be observed to slightly overpredict the intensity of secondary structures, by and large, the computational and experimental results are found to agree reasonably well.

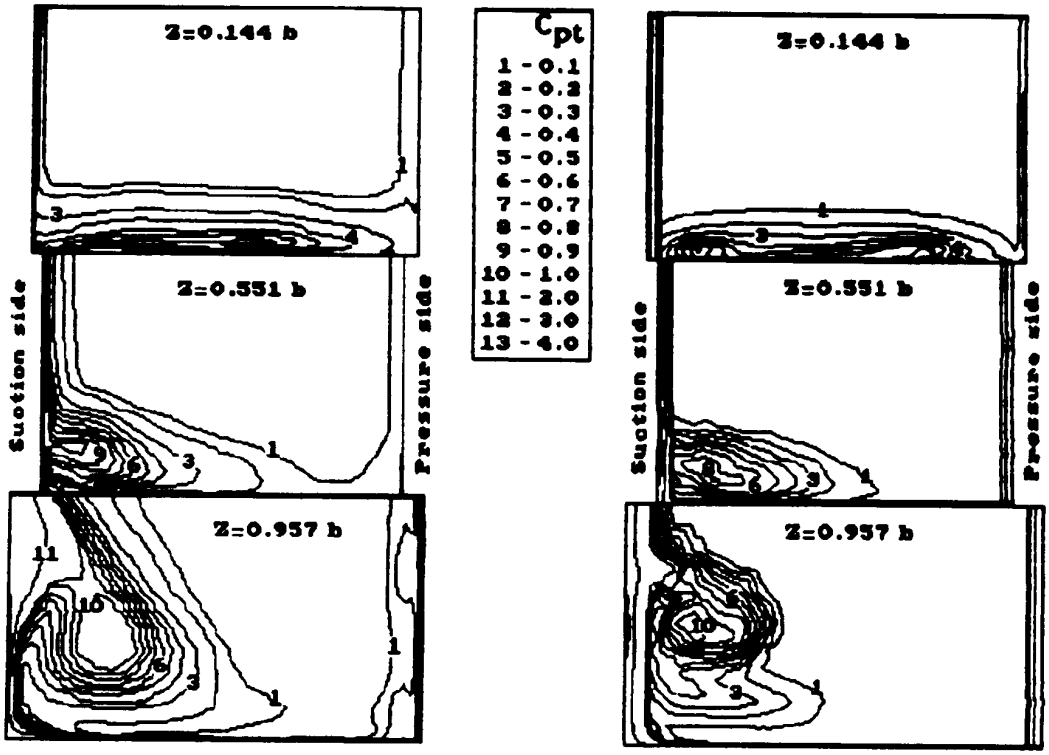

Fig.7. Langston cascade - computed (left) and experimental (right) contours of the total pressure coefficient at subsequent cross-flow sections of the blade-to blade passage.

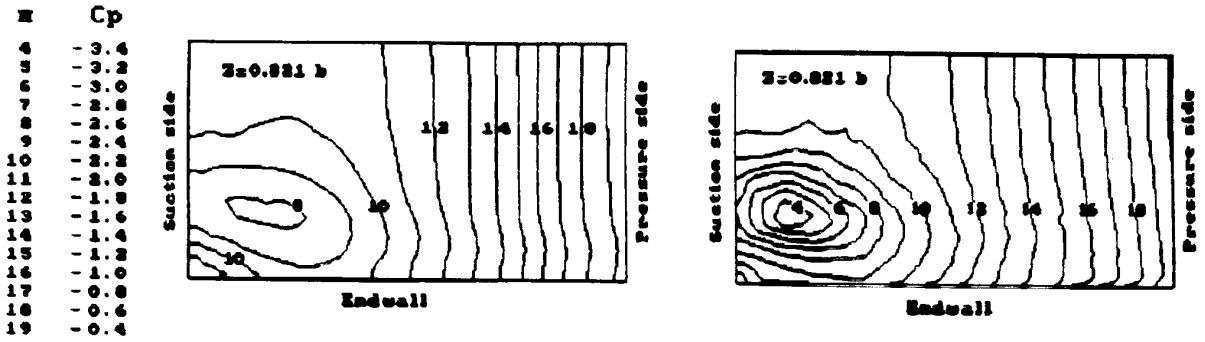

Fig.8. Langston cascade - computed (left) and experimental (right) contours of the static pressure coefficient at subsequent cross-flow sections of the blade-to blade passage.

Hodson & Dominy cascade

The next example is a 3D linear cascade of Hodson & Dominy [12]. Fig. 9 shows calculated velocity vectors at the pressure side and suction side of the blade. The positions of separations and reattachments are shown schematically by dashed lines ***S*** and ***R***, respectively. The span-wise distribution of the total pressure loss coefficient near the exit (2% axial chord downstream of the trailing edge) and in the region of wake (10 and 42 % axial chord downstream of the trailing edge) is presented in Fig. 10. The picture contains results of our computations (solid lines) together with the results of experimental investigations of Hodson & Dominy (circles) and results of numerical calculations of Ivanow & Krupa [13], based on the TVD method (dashed lines).

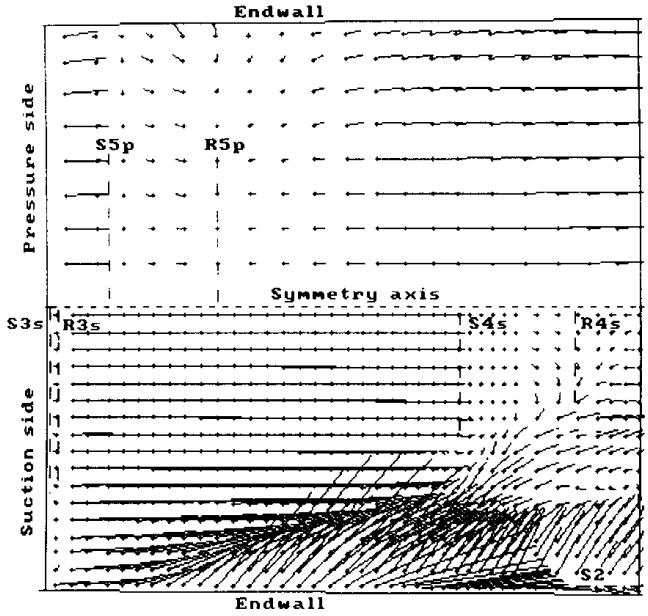

Fig. 9. Hodson & Dominy cascade - computed velocity vectors at the pressure side and suction side of the blade.

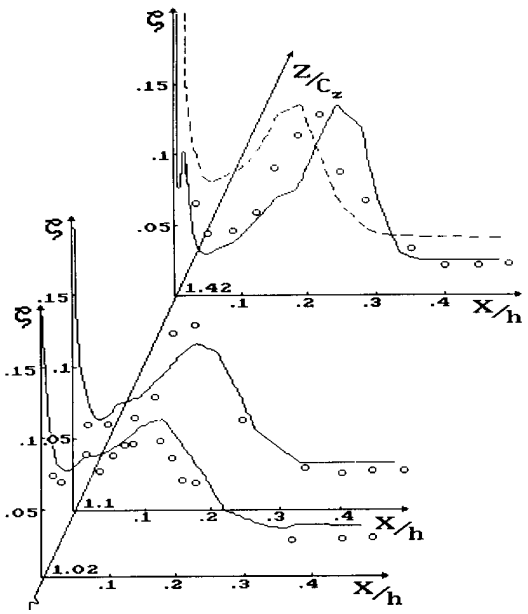

Fig. 10. Hodson & Dominy cascade - span-wise distribution of the total pressure loss coefficient at several distances from the trailing edge.

The comparison of computational and experimental velocity vectors and total pressure contours at the exit section from the cascade is presented in Fig. 11. The symbols A, B, C mark respectively the corner, passage and discrete vortices. As in the case of the Langston cascade, it seems that the numerical method tends to slightly overpredict the intensity of secondary structures. However, there is still good agreement in quality and quantity between computational and experimental figures.

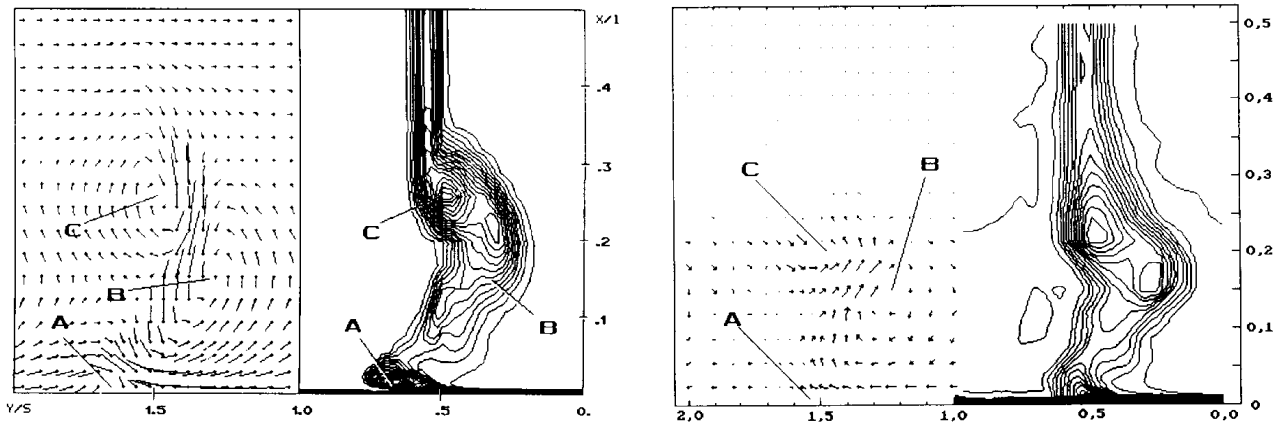

Fig. 11. Hodson & Dominy cascade - the comparison of computational and experimental velocity vectors and total pressure contours at the exit section.

Model air turbine

The final example is a model air turbine of ITC £ódŸ [23]. The geometric and thermodynamic characteristics of this two-row stator-rotor stage are displayed in Tab. 1. A 3D view of the calculation grid for the stator and rotor is shown in Fig. 12. The computational area consists of 420 000 cells in total. Figs. 13 and 14 present the obtained contours of total pressure and entropy function behind the stator and rotor. The shape of the wake behind the stator and rotor seems to be regular for that type of flow. Local maxima of the entropy function due to secondary vortices are clearly visible at some distances from the endwalls.

	stator	rotor
span/chord l/b	0.73	2.20
pitch/chord t/b	0.86	0.80
span/diameter l/D	0.08	0.08
stagger angle [deg]	47	13.6
pressure drop	0.9	
inlet temp. [^{o}C]	320	
flow rate [kg/s]	4.3	
average reaction	0.23	
efficiency	0.87	

Tab.1. Approximate geometric and thermodynamic characteristics of a model air turbine stage.

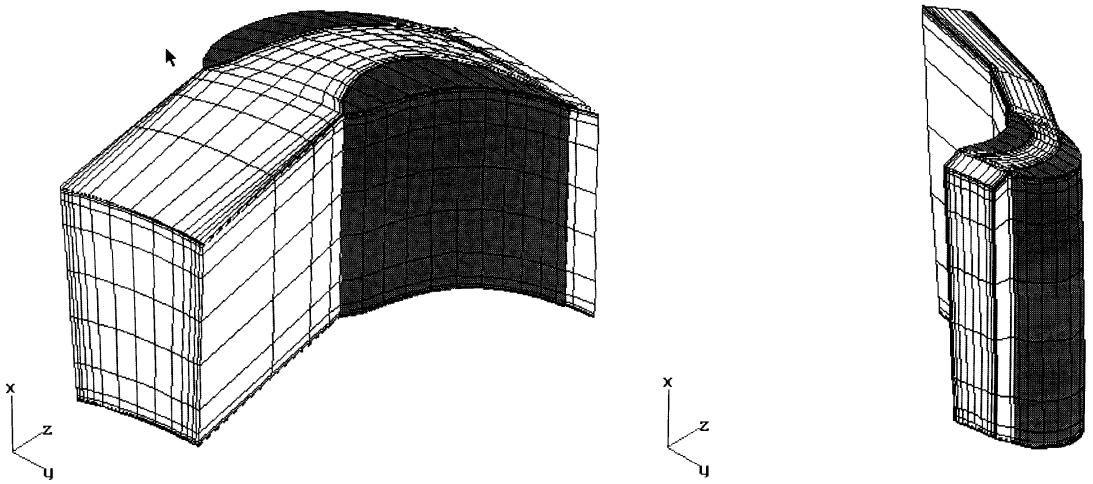

Fig. 12. Model air turbine - the calculation grid for the stator (left) and rotor (right).

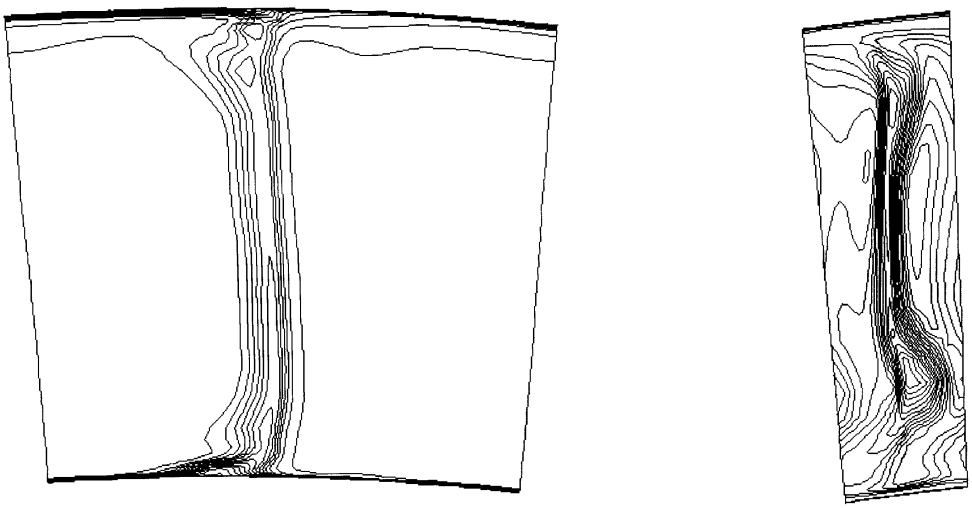

Fig. 13. Model air turbine - computed contours of total pressure behind the stator (left) and rotor (right).

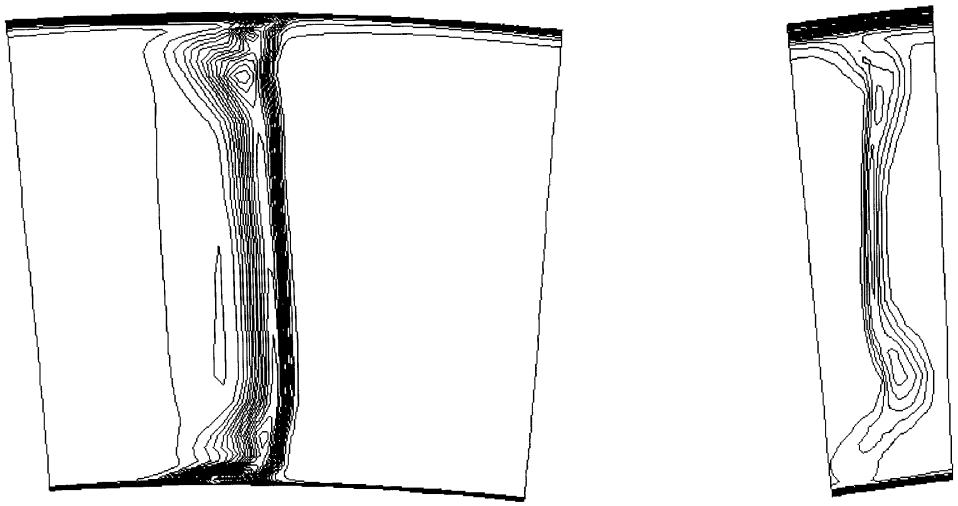

Fig. 14. Model air turbine - computed contours of entropy function behind the stator (left) and rotor (right).

The computed overall efficiency η_u of the flow that includes kinetic energy losses - profile and endwall losses, wake and exit velocity - is equal to 0.87, for the optimum load (u/c_{0t}=0.54). The comparison of computational and experimental efficiency characteristics as a function of load is presented in Fig. 15. In the same picture, there is a comparison of the computed and measured degree of reaction at the hub ρ_W and casing ρ_Z. A small table attached to Fig. 15 gives a set of discrete values of the above mentioned global characteristics of the stage for three values of load. Except for ρ_Z, other computed characteristics compare well with those obtained from the experiments. Most likely, a reason for the discrepancy in ρ_Z is that the numerical scheme does not incorporate tip leakage regions.

Another comparison of experimental and computational results is presented in Figs. 16a-c. These picture concern the span-wise distribution of velocity and yaw angle at the exit from the stage for three values of load. Although the results may not agree in quantity near endwalls, the character of the computed curves is a decent reproduction of experimental values.

u/c_{0t}	0.45	0.54	0.65
η_u	0.856	0.872	0.847
ρ_w	0.07	0.14	0.18
ρ_z	0.14	0.21	0.25

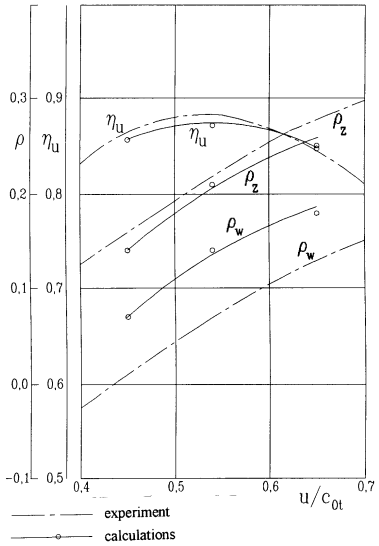

Fig. 15. Model air turbine - computed (solid lines) and experimental (dash-dotted lines) efficiency and reaction characteristics of the stage as a function of load.

The presented computations were carried out for subsonic flows. The numerical scheme also lends itself to the calculation of transonic and supersonic flows. To see some other examples of computations with the help of the presented numerical method the reader is requested to refer to [6,7,8,31,32].

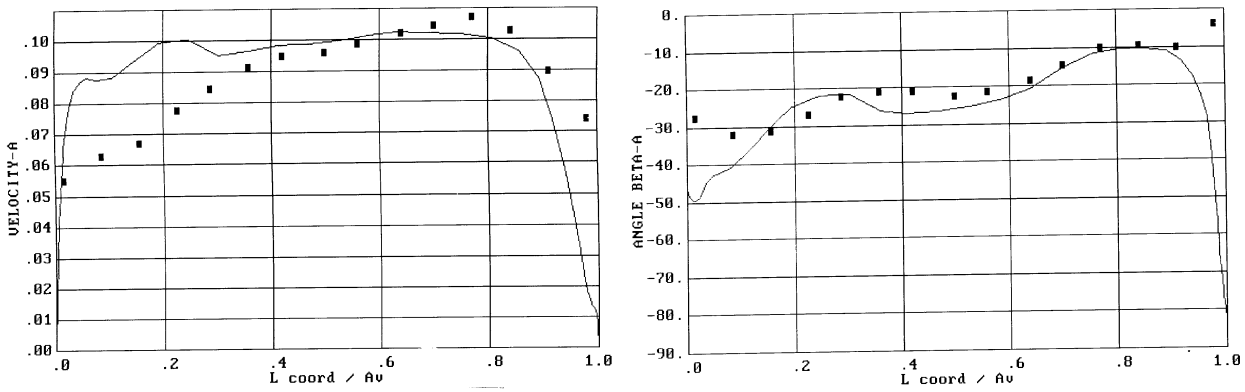

Fig. 16a. Model air turbine - the comparison of computed (solid lines) and experimental (rectangular points) velocities (left) and yaw angles (right) at the exit from the rotor for u/c_{0t}=0.45.

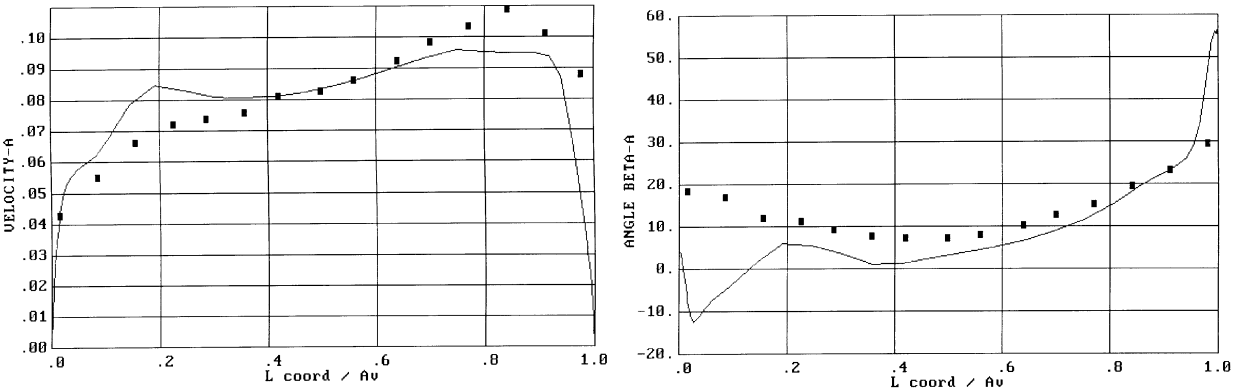

Fig. 16b. Model air turbine - the comparison of computed (solid lines) and experimental (rectangular points) velocities (left) and yaw angles (right) at the exit from the rotor for u/c_{0t}=0.54.

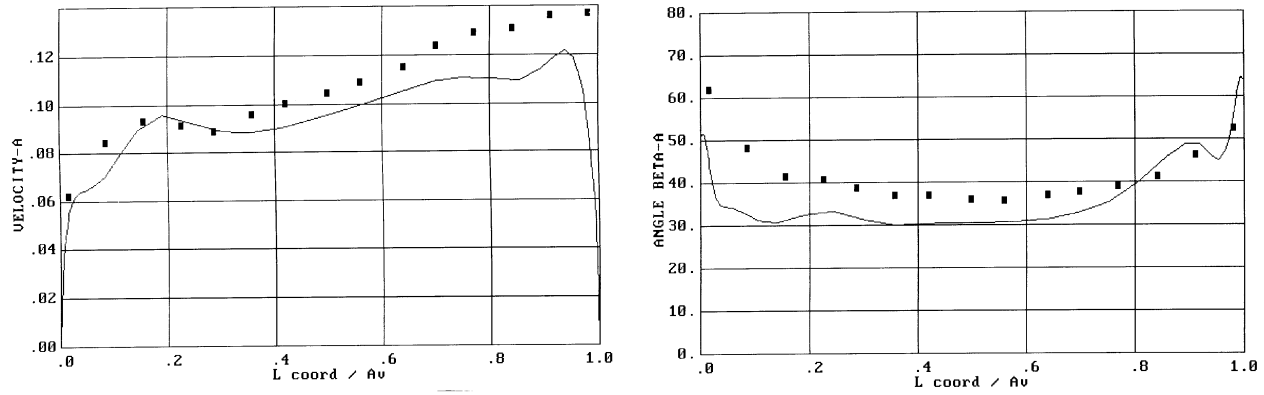

Fig. 16c. Model air turbine - the comparison of computed (solid lines) and experimental (rectangular points) velocities (left) and yaw angles (right) at the exit from the rotor for u/c_{0t}=0.65.

Conclusions

A numerical method to solve 3D turbomachinery flows is described in the paper. The governing equations are assumed in the form of thin-layer Reynolds-averaged Navier-Stokes equations. The effects of turbulence are incorporated with the help of a modified Baldwin-Lomax model. The numerical procedure is constructed based on the upwind difference Godunov scheme. An increased accuracy of calculations is achieved thanks to the applied ENO approximation of derivatives of characteristic variable derivatives. The scheme is locally third-order accurate and does not degenerate below the second-order accuracy anywhere in space and time.

The presented examples of computations concern single 3D cascades and a two-row model air turbine. The computational results reproduce well main structures of the flow characteristic for the tested range of Mach numbers and aspect ratios (blade span/pitch, chord/pitch). The presented illustrations exhibit the occurrence of horseshoe vortices, passage and corner vortices, development of secondary flows, presence of wakes, separations and reattachments. Thanks to post-processing of computed flow characteristics, the computer code enables the determination of global characteristics of axial machines, including stage efficiency and reaction that also remain within reasonable agreement with results of experimental investigations. The elaborated code seems to be suitable not only for investigating 3D flow phenomena in turbomachines but also can be instrumental in engineering practice to help design high performance blading for HP, MP, LP turbines and compressors.

References

[1] Baldwin B.S., Lomax H., *Thin layer approximation and algebraic model for separated turbulent flows*, AIAA Paper No 257 (1978).

[2] Beam R.M., Warming R.F., *An implicit factored scheme for the compressible Navier-Stokes equations*, AIAA J. 16 (1978) No 4.

[3] Chakravarthy S.R., Szema K.Y., Goldberg V.C., Gorski J.J., *Application of a new class of high accuracy TVD schemes to the Navier-Stokes equations*, AIAA Paper No 165 (1985).

[4] Colantuoni S., Terlizzi A., Grasso F., *A validation of a Navier-Stokes 2D solver for transonic turbine cascade flows*, AIAA Paper No 2451 (1989).

[5] Fletcher C.A.J., *Computational Techniques for Fluid Dynamics 2. Specific Techniques for Different Flow Categories*, Springer-Verlag Berlin, Heidelberg 1988.

[6] Gardzilewicz A., Rusanov A.V., Yershov S.V., Gnesin V., *Analysis of prospects of raising the efficiency of LP stages of steam turbines with the help of 3D computations*, Rep. Diagnostyka Maszyn Ltd., Gdañsk, 31 (1995) (in Polish).

[7] Gardzilewicz A., Yershov S.V., Rusanov A.V., Lampart P., *Study of prospects of raising the efficiency of impulse turbine stages with the help of 3D computations*, Rep. Diagnostyka Maszyn Ltd., Gdañsk, Part 1. - 18 (1996), Part 2. - 25 (1996) (in Polish).

[8] Gardzilewicz A., Yershov S.V., Rusanov A.V., Lampart P., Kietliñski K., Elszkowski J., *Increasing the efficiency of cylindrical stages of impulse turbines with the help of 3D flow computations*, Proc. Int. Conf. Modelling & Design in Fluid-Flow Machinery IMP'97, November 18-21, 1997.

[9] Godunov S.K., Zabrodin A.W., Ivanov M.A., *Solving multidimensional problems in gas dynamics*, Nauka, Moscow, 1976 (in Russian).

[10] Harten A., *High resolution schemes for hyperbolic conservation laws*, J. Comp. Phys. 49 (1983) No 3.

[11] Harten A., Osher S., *Uniformly high-order accurate non-oscillatory schemes*, SIAM Journal of Numerical Analysis 24 (1987) No 2.

[12] Hodson H.P., Dominy R.G., *Three-dimensional flow in a low-pressure turbine cascade at its design condition*, J. Turbomachinery 109 (1987) No 2.

[13] Ivanov M.A., Krupa V.G., *Computation of 3D viscous cascade f low*, News of Russian Academy of Sci., Fluid & Gas Mechanics, 1993 No 4.

[14] Ivanov M.A. Nigmatulin P.Z., *Implicit Godunov scheme of increased accuracy for integration of Euler equations*, J. Math. and Math. Phys. 6 (1989) (in Russian).

[15] Kinsey D.W., Eastep F.E., *Navier-Stokes solution for a thick supercritical airfoil with strong shocks and massively separated flow*, AAIA Paper No 0706 (1988).

[16] Kolgan W.P., *Numerical schemes for solving problems in gas dynamics*, Proc. Aerodynamics Inst. 3 (1972) No 6 (in Russian).

[17] Langston L.S., Nice M.L., Hopper R.M., *Three-dimensional flow within a turbine blade cascade*, Trans. ASME J. Power Engng 99 (1977) No 1.

[18] Liu F., Jameson A., *Multigrid Euler calculations for three-dimensional cascade*, AIAA Paper No 688 (1990).
[19] MacCormack R.W., *The effect of viscosity in hypervelocity impact cratering*, AIAA Paper No 354 (1969)
[20] Ramsey C.L., Anderson W.K., *Some numerical and physical aspects of unsteady Navier-Stokes computations over airfoils using dynamic meshes*, AIAA Paper No 247 (1986)
[21] Rody W., Srinivas K., *Computation of flow and losses in transonic turbine cascades*, Z. Fluwiss. Weltraumforsch, No 13 (1989).
[22] Tiliaeva N.I., *Modification of Godunov scheme on arbitrary non-structured grids*, Proc. Aerodynamics Inst., 17 (1986) No 2 (in Russian).
[23] Wiechowski S., *Results of investigations of annular cascades TK8, TK9 and models TK8-TW3, TK9-TW3*, Rep. Institute of Thermal Engng £ódŸ, 1988 (in Polish).
[24] Yershov S.V., *Simulation of separated viscous flows using the implicit monotonicity-preserving high-resolution Godunov scheme*, Int. Conf. Methods of Aerophysical Researches, Novosibirsk, Russia (1992).
[25] Yershov S.V., *The quasi-monotonous ENO scheme of increased accuracy for integrating Euler and Navier-Stokes equations*, Mathematical Modelling 6 (1994) No 11 (in Russian).
[26] Yershov S.V., Rusanov A.V., *3D separated viscous flow calculation using Godunov's high resolution scheme*, Int. Conf. Methods of Aerophysical Researches, Novosibirsk, Russia, 1994.
[27] Yershov S.V., Rusanov A.V., *The high resolution method of Godunov's type for 3D viscous flow calculations,* Proc. 3rd Colloq. Process Simulation, Espoo, Finland, 1996.
[28] Yershov S.V., Rusanov A.V., *The new implicit ENO method for 3D viscous multi stage flow calculations. Computational Fluid Dynamics '96,* Proc. 3rd ECCOMAS Computational Fluid Dynamics Conf., Paris, France, September 9-13, 1996.
[29] Yershov S.V., Rusanov A.V., *The application package FlowER for the calculation of 3D viscous flows through multi-stage turbomachinery*, Certificate of state registration of copyright, Ukrainian state agency of copyright and related rights, February 19, 1996.
[30] Yershov S.V., Rusanov A.V., *Modification of algebraic turbulence model used in code FlowER*, In Modelling Turbulence in Technical Applications, Copybooks of Institute of Fluid-Flow Machinery, Gdañsk, Poland, 486 (1997).
[31] Yershov S.V., Rusanov A.V., Gardzilewicz A., Badur J., Lampart P., *Calculations of Test Case 3 - Durham low speed turbine cascade*, Proc. V ERCOFTAC Seminar and Workshop on 3D Turbomachinery Flow Prediction, Courchevel, France, January 6-9, 1997.
[32] Yershov S.V., Rusanov A.V., Gardzilewicz A., Badur J., Lampart P., *Calculations of Test Case 9 - Highly loaded transonic linear turbine guide vane cascade*, Proc. V ERCOFTAC Seminar and Workshop on 3D Turbomachinery Flow Prediction, Courchevel, France, January 6-9, 1997.